

Theoretical study of orientation-dependent multiphoton ionization of polyatomic molecules in intense ultrashort laser fields: A new time-dependent Voronoi-cell finite difference method

Sang-Kil Son^a, Shih-I Chu^{a,b}

^a*Department of Chemistry, University of Kansas, Lawrence, Kansas 66045, USA*

^b*Center for Quantum Science and Engineering, Department of Physics, National Taiwan University, Taipei 10617, Taiwan*

Abstract

We present a new grid-based time-dependent method to investigate multiphoton ionization (MPI) of polyatomic molecules in intense ultrashort laser fields. The electronic structure of polyatomic molecules is treated by the density-functional theory (DFT) with proper long-range potential and the Kohn–Sham equation is accurately solved by means of the Voronoi-cell finite difference method on non-uniform and highly adaptive molecular grids utilizing geometrical flexibility of the Voronoi diagram. This method is generalized to the time-dependent problems with the split-operator time-propagation technique in the energy representation, allowing accurate and efficient non-perturbative treatment of attosecond electronic dynamics in strong fields. The new procedure is applied to the study of MPI of N₂ and H₂O molecules in intense linearly-polarized and ultrashort laser fields with arbitrary field–molecule orientation. Our results demonstrate that the orientation dependence of MPI is determined not just by the highest-occupied molecular orbital (HOMO) but also by the symmetries and dynamics of other contributing molecular orbitals. In particular, the inner orbitals can show dominant contributions to the ionization processes when the molecule is aligned in some specific directions with respect to the field polarization. This feature suggests a new way to selectively probe individual orbitals in strong-field electronic dynamics.

Key words: Voronoi-cell finite difference method, multiphoton ionization, orientation dependence, polyatomic molecules, strong-field dynamics, attosecond, time-dependent density-functional theory, nitrogen, water, VFD, TDVFD, MPI, TDDFT, N₂, H₂O

PACS: 33.80.Rv, 31.15.A-, 31.15.E-

1. Introduction

The study of attosecond physics and chemistry in intense ultrashort laser fields is a subject of much current significance in science and technology [1, 2]. Attosecond pulses can be produced by means of high harmonic generation (HHG) of atoms in intense laser fields [3, 4] and the time profile of the attosecond pulses can be controlled by tuning the carrier envelope phase [5, 6]. Recent progress of attosecond physics includes control of electron wave packets [7], probing of nuclear dynamics [8] and electronic dynamics [9], attosecond time-resolved spectroscopy [10], and tomographic imaging of molecular orbitals [11], etc. One of the most novel features in an attosecond time scale is the direct observation of the motion of electrons in atoms and molecules [12]. And the exploration of the attosecond electronic dynamics in the strong-field regime has attracted much interest theoretically and experimentally.

The multiphoton ionization (MPI) of molecules in intense laser fields is one of the fundamental processes in attosecond and strong-field phenomena. Most of the recent theoretical studies of MPI are based on approximated models

such as the molecular Ammosov–Delone–Krainov (ADK) [13] and Keldysh–Faisal–Reiss [14] models, which usually consider only the highest-occupied molecular orbital (HOMO) contribution and neglect the multi-electron dynamics from multiple orbitals. However, there have been several recent experimental studies showing significant discrepancies between experimental observations and approximated models, for examples, the non-suppression of F₂ MPI [15, 16] and the orientation dependence of CO₂ MPI [17, 18], etc. More recently, the importance of contribution to HHG and MPI from the inner orbital just below HOMO has been experimentally demonstrated in diatomic N₂ [19] and polyatomic N₂O₄ [20], which cannot be explained by the approximated models. Thus, it is an important and timely task to develop more comprehensive and accurate theoretical description of strong-field electronic dynamics including electron correlation and multi-electron responses. Along this direction, we note that the *self-interaction-free* time-dependent density-functional theory (TDDFT) has been recently developed and successfully applied to a number of studies of atomic and diatomic molecular processes in intense laser fields [21–25], with results in good agreement with experiments.

We note that besides the TDDFT approach, several other time-dependent approaches such as time-dependent configura-

Email addresses: sangkil@ku.edu (Sang-Kil Son), sichu@ku.edu (Shih-I Chu)

tion interaction (TDCI) [26] and multi-configurational time-dependent Hartree–Fock (MCTDHF) [27] methods have been recently proposed. However, most of these recent studies have been applied to either one-dimensional model systems or consider only the transitions among the bound states without including the continuum spectrum and ionization problems. Indeed, accurate study of strong-field ionization in polyatomic molecular systems, taking into account both electron correlation and multiple orbital responses, remains a grand challenging problem in strong-field molecular physics. In this paper, we consider the extension of the TDDFT approach with proper long-range potential to the *ab initio* nonperturbative study of multiphoton ionization of polyatomic molecules in intense laser fields.

From the numerical aspect, the multi-center Coulombic singularity is a key bottleneck for the accurate treatment of electronic structure and dynamics in polyatomic molecules. The Coulombic potential ($-1/r$) incorporates cusps at nuclear positions in electronic bound states and also influences continuum states that are crucial in strong-field electronic dynamics. The commonly used equal-spacing grid methods [28] are not adequate to handle the short- and long-range of the Coulombic potential. To address this issue, a numerical grid-based method requires local grid refinement around nuclei, such as non-uniform grids that are distributed denser near nuclei and sparser away from nuclei. For atomic and diatomic systems, Chu and collaborators [21, 29–31] have developed the time-dependent generalized pseudospectral (TDGPS) method on non-uniform and optimal grids to accurately solve the electronic structure and strong-field quantum dynamics with the realistic Coulombic potential by use of the spherical coordinates (for atoms) and the prolate spheroidal coordinates (for diatomic molecules). In this paper, we present a new and different numerical procedure for polyatomic molecular systems based on highly adaptive molecular grids, regardless of the coordinate system and molecular symmetry.

To accurately solve the Schrödinger equation on highly adaptive molecular grids, we can employ the Voronoi diagram [32]. The Voronoi diagram has tremendous applications [33, 34] over one century because of its attractiveness and versatility of geometry. One of noticeable applications for numerical analysis is the natural element method (NEM) [35–37] taking geometrical advantages of the Voronoi diagram. As a simpler form of NEM, Sukumar and colleagues [38, 39] recently proposed the Voronoi-cell finite difference (VFD) method for numerical solutions of the Poisson equation on arbitrarily distributed grids. In contrast to the ordinary finite difference method with regular uniform grids, this method can accommodate any types of grid distributions. Since there is no restriction on the locations of grid points, VFD is regarded as a meshfree (or meshless) method which is of current interest in numerical analysis [40, 41]. More recently, the VFD method was extended to the Schrödinger equation solver for polyatomic molecular calculations [42].

In this paper, we present a new time-dependent Voronoi-cell finite difference (TDVFD) method for the accurate and efficient solution of time-dependent Schrödinger and Kohn–Sham equa-

tions, combining with the split-operator technique in the *energy* representation [29, 30]. Then we shall apply the proposed numerical method to the all-electron TDDFT calculation (with proper long-range potential) for the investigation of strong-field multiphoton electronic dynamics in diatomic and small polyatomic molecules, taking into account electron correlation and multi-electron responses.

The outline of this paper is as follows. In Sec. 2, we discuss the Laplacian and gradient operators in the VFD method, especially for the solution of the Schrödinger equation, and then introduce a new TDVFD method. We also propose highly adaptive molecular grids suitable for polyatomic molecular calculations. In Sec. 3, we present the electronic structures of several small polyatomic molecules with *self-interaction-free* DFT computed by the VFD method. In Sec. 4, we extend the TDVFD method to the solution of TDDFT equations to investigate the orientation dependence of MPI of N_2 and H_2O in intense and ultrashort laser pulses. This is followed by a conclusion in Sec. 5.

2. Time-dependent Voronoi-cell finite difference method

2.1. Discrete Laplacian operator

The discrete Laplacian operator in the Voronoi-cell finite difference (VFD) scheme was proposed by Sukumar and colleagues [38, 39]. In this section, we briefly review the derivation of the Laplacian matrix in the VFD scheme.

Given an arbitrarily distributed grid-point set $\{\mathbf{r}_i\}$ in n -dimensions, a Voronoi cell surrounding a grid of \mathbf{r}_i is defined by a set of points that are closer to \mathbf{r}_i than to any other grids [33],

$$T_i = \{\mathbf{r} \in \mathbb{R}^n : d(\mathbf{r}, \mathbf{r}_i) \leq d(\mathbf{r}, \mathbf{r}_j) \text{ for } \forall j \neq i\}, \quad (1)$$

where $d(\mathbf{r}_i, \mathbf{r}_j)$ is a distance between two points \mathbf{r}_i and \mathbf{r}_j . It is well known that the Voronoi diagram is uniquely defined for a given grid-point set [33]. Thus the Voronoi diagram provides an unique discretization of the whole space. Figure 1 shows one example of a Voronoi diagram in the 2-dimensional (2D) case. T_i indicates the Voronoi cell encapsulating the i -th grid, and its volume is given by v_i . A Voronoi facet, s_{ij} , is the surface where two adjacent T_i and T_j meet together. Note that the Voronoi facet is a line in 2D (also called the Voronoi edge) as shown in Fig. 1 and a plane in 3D. h_{ij} is a distance between the i -th and j -th grids. From the Voronoi properties, s_{ij} is the perpendicular bisector of h_{ij} . A natural neighbor [43] is defined by the fact that if two grids share a common Voronoi facet, they are natural neighbors. For example, in Fig. 1 the grids of 1–5 are natural neighbors of the i -th grid but the grid of 6 is not. A Voronoi vertex is defined as the point where Voronoi facets converge. In other words, the Voronoi facet between two neighboring grids is surrounded by Voronoi vertices belonging to the two grids. Therefore, an area of s_{ij} in 3D (or a length in 2D) can be computed using the position of the surrounding vertices. T_i is further decomposed into polygonal pyramids that have their apex at the i -th grid and their base as each Voronoi facet, so v_i can be computed by the sum of volumes of these polygonal pyramids. To summarize, for a given set of arbitrarily distributed grids, v_i ,

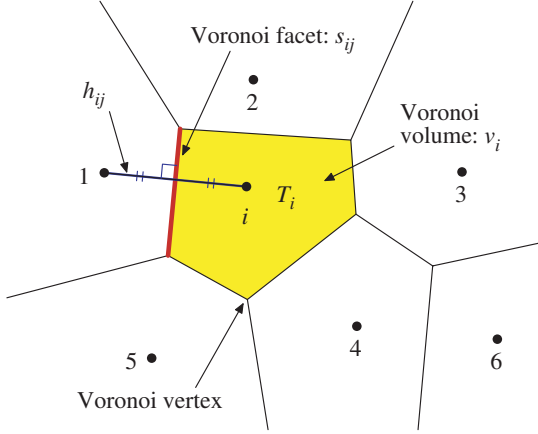


Figure 1: (Color online) Voronoi diagram on arbitrarily distributed grid points

s_{ij} , and h_{ij} are easily calculated by Voronoi vertices and natural neighboring relations within the Voronoi diagram. For numerical determination of the Voronoi diagram, we use the Qhull package [44], and all calculations are performed in 3D.

The Gauss's theorem [45] states that

$$\int_V \nabla \cdot \mathbf{F} dV = \int_S \mathbf{F} \cdot \mathbf{n} dS. \quad (2)$$

From this theorem, the Laplacian acts on a function φ is defined in the integral form,

$$\nabla^2 \varphi = \lim_{\int_V dV \rightarrow 0} \frac{\int_S \nabla \varphi \cdot \mathbf{n} dS}{\int_V dV}, \quad (3)$$

where \mathbf{n} is the normal vector of the surface S . After the Voronoi discretization, the volume in the vicinity of the i -th grid can be given by the Voronoi cell, T_i . Then the volume integral is converted into the Voronoi volume, v_i , and the surface integral is decomposed into the areas of the Voronoi facets, s_{ij} , over neighboring grid j 's. The inner product indicates a directional derivative of φ , which can be approximated by the simple difference scheme, $(\nabla \varphi)_i \cdot \mathbf{n}_{ij} \approx (\varphi_j - \varphi_i)/h_{ij}$, since h_{ij} is perpendicular to s_{ij} . Thus the discrete Laplacian at the i -th grid in the VFD scheme can be evaluated by [38, 39],

$$(\nabla^2 \varphi)_i = \frac{1}{v_i} \sum_j^{\text{neighbors}} \frac{\varphi_j - \varphi_i}{h_{ij}} s_{ij}. \quad (4)$$

Once v_i , s_{ij} , and h_{ij} for given grid points are available, one can simply compute the Laplacian in the framework of VFD. The matrix form of the Laplacian operator \mathbf{L} in VFD is expressed as

$$\mathbf{L} : L_{ij} = \begin{cases} -\frac{1}{v_i} \sum_k^{\text{neighbors}} \frac{s_{ik}}{h_{ik}} & (i = j), \\ \frac{1}{v_i} \frac{s_{ij}}{h_{ij}} & (i, j: \text{neighbors}), \\ 0 & (\text{otherwise}), \end{cases} \quad (5)$$

where k runs over natural neighbors of the i -th grid. Note that \mathbf{L} is not symmetric ($L_{ij} \neq L_{ji}$) due to v_i .

This VFD scheme resembles the finite volume method (FVM) [46] in the sense that both are based on the Gauss's theorem and cell volumes to derive basic formula. However, VFD substitutes the volume integral with the Voronoi volume and the surface integral with the simple finite difference form of the directional derivatives, while FVM generally evaluates those integrals using interpolation and quadrature. As a result, VFD provides the simple and explicit expressions at each grid without additional background grids.

2.2. Symmetrized VFD Hamiltonian for the time-independent Schrödinger equation

In this section, we discuss how to solve the time-independent Schrödinger equation with the symmetrized VFD Hamiltonian matrix [42]. One can directly use the discrete Laplacian operator in VFD to solve the Schrödinger equation for one electron,

$$\left[-\frac{1}{2} \nabla^2 + u(\mathbf{r}) \right] \psi(\mathbf{r}) = \varepsilon \psi(\mathbf{r}), \quad (6)$$

where $u(\mathbf{r})$ is a potential function, $\psi(\mathbf{r})$ is an eigenfunction, and ε is an eigenvalue. Note that the atomic units are used throughout the paper, unless otherwise indicated. The reduced mass of the electron is set to the unity. In the matrix representation, the Hamiltonian matrix is given by

$$\mathbf{H} = -\frac{1}{2} \mathbf{L} + \mathbf{U}, \quad (7)$$

where \mathbf{U} is a potential matrix and given by diagonal elements evaluated at each grid,

$$\mathbf{U} : U_{ij} = \delta_{ij} u(\mathbf{r}_i). \quad (8)$$

Then, the eigenvalue problem to be solved is

$$\mathbf{H}\mathbf{C} = \mathbf{C}\mathbf{E}, \quad (9)$$

where \mathbf{C} is the eigenvector matrix and \mathbf{E} is the diagonal matrix of eigenvalues. Since \mathbf{L} is non-symmetric, it is advantageous to transform \mathbf{H} into a symmetric form to facilitate the eigenvalue solution.

Here we introduce a transformation of $\tilde{\mathbf{C}} = \mathbf{V}^{\frac{1}{2}} \mathbf{C}$ where \mathbf{V} is given by diagonal elements of Voronoi volumes,

$$\mathbf{V} : V_{ij} = \delta_{ij} v_i. \quad (10)$$

When $\mathbf{C} = \mathbf{V}^{-\frac{1}{2}} \tilde{\mathbf{C}}$ is substituted into Eq. (9), one obtains

$$\left(-\frac{1}{2} \mathbf{V}^{\frac{1}{2}} \mathbf{L} \mathbf{V}^{-\frac{1}{2}} + \mathbf{U} \right) \tilde{\mathbf{C}} = \tilde{\mathbf{C}} \mathbf{E}, \quad (11)$$

where $\mathbf{V}^{\frac{1}{2}} \mathbf{U} \mathbf{V}^{-\frac{1}{2}} = \mathbf{U}$ is used because both \mathbf{U} and \mathbf{V} are diagonal matrices. Using a similarity transformation of \mathbf{L} ,

$$\tilde{\mathbf{L}} = \mathbf{V}^{\frac{1}{2}} \mathbf{L} \mathbf{V}^{-\frac{1}{2}}, \quad (12)$$

one obtains a symmetric matrix $\tilde{\mathbf{L}}$. The explicit expressions for $\tilde{\mathbf{L}}$ elements are

$$\tilde{\mathbf{L}} : \tilde{L}_{ij} = \begin{cases} -\frac{1}{v_i} \sum_k^{\text{neighbors}} \frac{s_{ik}}{h_{ik}} & (i = j), \\ \frac{1}{\sqrt{v_i v_j}} \frac{s_{ij}}{h_{ij}} & (i, j: \text{neighbors}), \\ 0 & (\text{otherwise}). \end{cases} \quad (13)$$

Note that VFD provides a very sparse matrix because it consists of diagonal elements and nonzero elements only at natural neighboring indexes.

Now one can solve the symmetric eigenvalue problem with $\tilde{\mathbf{H}} = -\frac{1}{2}\tilde{\mathbf{L}} + \mathbf{U}$ instead of Eq. (9),

$$\tilde{\mathbf{H}}\tilde{\mathbf{C}} = \tilde{\mathbf{C}}\mathbf{E}. \quad (14)$$

The eigenvalues of this real symmetric sparse matrix are numerically determined by the implicitly restarted Lanczos method of ARPACK [47] and the large sparse matrix solver of PARISO [48].

When a numerical integral is required, for examples, computation of energy functionals in Sec. 3.1 or ionization probability in Sec. 4.1, a set of Voronoi volumes, $\{v_i\}$, works as weights in the nodal quadrature method [49] without additional background cells or grids. The integral in the VFD scheme is simply evaluated by the summation over all grids,

$$\int_V f(\mathbf{r})dV \approx \sum_i^{\text{all}} f(\mathbf{r}_i)v_i. \quad (15)$$

The numerical error of this nodal quadrature was analyzed elsewhere [42].

2.3. Discrete gradient operator

In this section, we derive a discrete gradient operator in the VFD scheme as the same manner as the Laplacian operator in Sec. 2.1. One can recall an alternative form of the Gauss's theorem [45],

$$\int_V \nabla f dV = \int_S f \mathbf{n} dS. \quad (16)$$

The gradient is defined in the integral form,

$$\nabla \varphi = \lim_{\int_V dV \rightarrow 0} \frac{\int_S \varphi \mathbf{n} dS}{\int_V dV}. \quad (17)$$

The gradient at the i -th grid is given by the summation over Voronoi facet areas divided by the Voronoi volume after the Voronoi discretization. To evaluate the surface integral over S , φ on S is approximated to $(\varphi_i + \varphi_j)/2$ on s_{ij} because s_{ij} is the perpendicular bisector of h_{ij} . Utilizing $\sum_j \mathbf{n}_{ij}s_{ij} = \mathbf{0}$ and the normal vector on s_{ij} by $\mathbf{n}_{ij} = (\mathbf{r}_j - \mathbf{r}_i)/h_{ij}$, one obtain the discrete gradient at the i -th grid in the VFD scheme as

$$\begin{aligned} (\nabla \varphi)_i &= \frac{1}{v_i} \sum_j^{\text{neighbors}} \frac{\varphi_j + \varphi_i}{2} \mathbf{n}_{ij}s_{ij} \\ &= \frac{1}{2v_i} \sum_j^{\text{neighbors}} \frac{\varphi_j s_{ij} (\mathbf{r}_j - \mathbf{r}_i)}{h_{ij}}. \end{aligned} \quad (18)$$

Note that this expression using the middle point of φ_i and φ_j is different from the gradient operator using the center of mass of the Voronoi facet [50]. The matrix form of the x -component of the gradient operator $\mathbf{G}^{(x)}$ is expressed as

$$\mathbf{G}^{(x)} : G_{ij}^{(x)} = \begin{cases} 0 & (i = j), \\ \frac{1}{2v_i} \frac{s_{ij}}{h_{ij}} (\mathbf{r}_j - \mathbf{r}_i) \cdot \hat{\mathbf{e}}_x & (i, j: \text{neighbors}), \\ 0 & (\text{otherwise}), \end{cases} \quad (19)$$

where $\hat{\mathbf{e}}_x$ is the unit vector of the x -axis. Also $\mathbf{G}^{(y)}$ and $\mathbf{G}^{(z)}$ are defined likewise. Note that the gradient operator is intrinsically non-symmetric.

2.4. TDVFD with the split-operator technique in the energy representation

In this section, we present a time-dependent Voronoi-cell finite difference (TDVFD) method as an extension of VFD to the time domain, incorporating with the second-order split-operator technique in the *energy* representation [29, 30]. Let us consider the time-dependent Schrödinger equation with a time-dependent potential $u(\mathbf{r}, t)$,

$$i \frac{\partial}{\partial t} \psi(\mathbf{r}, t) = \hat{H}(\mathbf{r}, t) \psi(\mathbf{r}, t), \quad (20)$$

where $\hat{H}(\mathbf{r}, t) = -\frac{1}{2}\nabla^2 + u(\mathbf{r}, t)$. For a numerical time-propagation of Eq. (20), $\hat{H}(\mathbf{r}, t)$ can be split into two parts as

$$\hat{H}(\mathbf{r}, t) = \hat{H}_0(\mathbf{r}) + \hat{U}(\mathbf{r}, t), \quad (21)$$

where

$$\hat{H}_0(\mathbf{r}) = -\frac{1}{2}\nabla^2 + u(\mathbf{r}, 0), \quad (22)$$

$$\hat{U}(\mathbf{r}, t) = u(\mathbf{r}, t) - u(\mathbf{r}, 0). \quad (23)$$

Here the unperturbed Hamiltonian $\hat{H}_0(\mathbf{r})$ is accurately solved by the VFD method and the time-dependent potential $\hat{U}(\mathbf{r}, t)$ is simply given by a diagonal matrix evaluated at each grid in the VFD scheme. Then the second-order split-operator technique for the time-propagation yields

$$\psi(t + \Delta t) = e^{-i\hat{U}(t)\frac{\Delta t}{2}} e^{-i\hat{H}_0\Delta t} e^{-i\hat{U}(t)\frac{\Delta t}{2}} \psi(t) + O(\Delta t^3), \quad (24)$$

where the coordinate \mathbf{r} is not explicitly expressed for brevity.

In the matrix representation,

$$\mathbf{f}(t + \Delta t) \leftarrow e^{-i\mathbf{U}(t)\frac{\Delta t}{2}} e^{-i\mathbf{H}_0\Delta t} e^{-i\mathbf{U}(t)\frac{\Delta t}{2}} \mathbf{f}(t), \quad (25)$$

where $\mathbf{f}(t)$ is a column vector of the time-dependent wavefunction represented in every grid,

$$\mathbf{f}(t) = (\cdots f_i(t) \cdots)^T; \quad f_i(t) = \psi(\mathbf{r}_i, t). \quad (26)$$

The exponential of the diagonal matrix is trivially obtained by exponentiating every entry on the main diagonal. Since $\mathbf{U}(t)$ is given by a diagonal matrix in VFD, $\exp(-i\mathbf{U}(t)\frac{\Delta t}{2})$ is simply computable. For $\exp(-i\mathbf{H}_0\Delta t)$, one defines an evolution matrix \mathbf{S} with the spectral decomposition of $\mathbf{H}_0 = \mathbf{C}\mathbf{E}\mathbf{C}^{-1}$,

$$\mathbf{S} = e^{-i\mathbf{H}_0\Delta t} = \mathbf{C}e^{-i\mathbf{E}\Delta t}\mathbf{C}^{-1}, \quad (27)$$

where $\exp(-i\mathbf{E}\Delta t)$ is easily computable with the eigenstate energies in the diagonal matrix \mathbf{E} .

For the symmetric Hamiltonian $\tilde{\mathbf{H}}_0$ in Eq. (14), the symmetric version is expressed by

$$\tilde{\mathbf{S}} = e^{-i\tilde{\mathbf{H}}_0\Delta t} = \tilde{\mathbf{C}}e^{-i\mathbf{E}\Delta t}\tilde{\mathbf{C}}^T, \quad (28)$$

and then the time-propagation is performed by

$$\tilde{\mathbf{f}}(t + \Delta t) = \mathbf{W}(t) \cdot \tilde{\mathbf{S}} \cdot \mathbf{W}(t) \cdot \tilde{\mathbf{f}}(t), \quad (29)$$

where $\tilde{\mathbf{f}} = \sqrt{2} \mathbf{f}$ and $\mathbf{W}(t) = e^{-i\mathbf{U}(t)\frac{\Delta t}{2}}$. All operations here are the matrix–vector multiplication and even $\mathbf{W}(t)$ is a diagonal matrix. The explicit expressions of the $\tilde{\mathbf{S}}$ elements are

$$\tilde{\mathbf{S}} : \tilde{S}_{ij} = \sum_k \tilde{C}_{ik} \tilde{C}_{jk} e^{-i\varepsilon_k \Delta t}, \quad (30)$$

where ε_k is the k -th eigenstate energy and \tilde{C}_{ik} is a value at the i -th grid of the k -th eigenvector of $\tilde{\mathbf{H}}$. We emphasize that this $\tilde{\mathbf{S}}$ is a time-independent complex symmetric matrix and it needs to be constructed only once before the time-propagation, which remarkably reduces the computation time.

This TDVFD scheme in the *energy* representation is different from the conventional split-operator techniques [51, 52] where \hat{H}_0 is usually chosen to be the kinetic energy operator solved by the fast Fourier transformation on the uniform grids. The advantages of using our proposed method are (i) highly adaptive molecular grids to solve \hat{H}_0 , which are to be discussed in the next section, and (ii) elimination of the undesirable fast-oscillating high-energy components in the $\tilde{\mathbf{S}}$ matrix [29, 30]. Both features allow us to reduce the number of spatial grids and to speed up the time-propagation considerably. Furthermore, this scheme inherits unconditionally numerical stability and conservation of probability from the original split-operator technique due to the unitary evolution operator [51]. Thus it conserves the norm of the wavefunctions during the time-propagation (for example, errors of the norm are about 10^{-10} in the field-free case), ensuring the numerical accuracy of ionization probabilities computed from the norm of the wavefunctions in Sec. 4.1.

2.5. VFD discretization for molecular systems

In the real-space grid method for polyatomic molecular calculations, local refinement around nuclear positions is requisite to capture the multi-center Coulomb singularity. Since the VFD scheme allows the freedom to choose any arbitrary grid distributions, i.e., calculations are performed on *unstructured*¹ grids, it may be possible to optimize molecular grids in a highly *structured*² manner. For polyatomic molecular grids, it is natural and intuitive to consider spherical atomic grids located at nuclear positions to attain more grids near the nuclei. In the previous work [42], we introduced three different types: non-overlap, overlap, and squeezed composite molecular grids. We concluded that non-overlap type would be better in accuracy and efficiency, which is constructed by the way that spherical atomic grids are combined and the grids in the overlapping region are removed except ones closest to the atom.

¹In numerical analysis, *unstructured* means that there is no fixed connectivity among grids, while *structured* means that there is a fixed number for connectivity among grids.

²Here, we use *structured* to express a well-designed grid distribution suitable for specific problems.

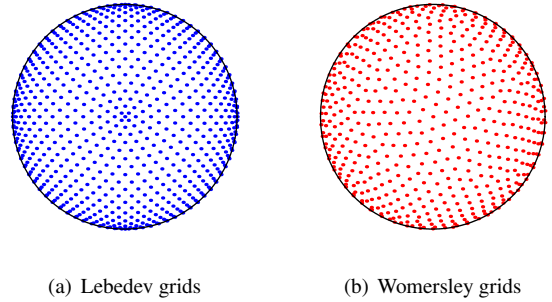


Figure 2: Comparison of two angular grid distributions plotted over the half sphere.

To achieve more local refinement in the vicinity of nuclei, the radial part of the spherical atomic grids with a finite maximum radius r_{\max} is generated by an algebraic mapping function [29],

$$r(x) = L \frac{1+x}{1-x + \frac{2L}{r_{\max}}} \quad (-1 < x \leq 1), \quad (31)$$

where L is a mapping parameter and x is defined as uniform grid points in 1D,

$$x_i = \frac{2i}{N_r} - 1 \quad (i = 1, \dots, N_r), \quad (32)$$

where N_r is the number of radial grids.

For the angular part of the spherical atomic grids, we adopt angular grid distributions from the Lebedev quadrature [53] and the Womersley quadrature [54]. Figure 2 compares the Lebedev and Womersley grid distributions for $l_{\max}=32$ that is the order of angular grids and also indicates the maximum angular momentum. The Lebedev grids retain the octahedral symmetry, so their distribution is to some extent biased around x , y , and z -axes. For a given l_{\max} , the number of angular grids is estimated by $N_{\text{ang}} \approx 4(l_{\max} + 1)^2/3$. On the other hand, the Womersley grids are designed to be fairly uniform over the sphere, and the number of angular grids is given by $N_{\text{ang}} = (l_{\max} + 1)^2$ exactly. Since numerical results of eigenvalues for both grid types show a very small difference ($\ll 5 \times 10^{-5}$ a.u. for $l_{\max}=10$) but the Womersley scheme offers the smaller N_{ang} , we shall use the Womersley grids for all calculations in this paper.

There are only four parameters to build up spherical atomic grids: N_r , L , and r_{\max} for the radial part, and l_{\max} for the angular part. Using the non-overlap scheme, we can construct molecular grids from the spherical atomic grids for the VFD calculations. Figure 3 shows 2D sketches of three examples of molecular grids: diatomic N_2 , linear triatomic CO_2 , and bent triatomic H_2O . One can observe that molecular grids are highly adaptive satisfying more grid points around nuclei.

3. Electronic structure calculation of polyatomic molecules by self-interaction-free density-functional theory

3.1. Application of VFD to density-functional theory

We apply the VFD method to accurately compute the electronic structure of many-electron polyatomic molecules using

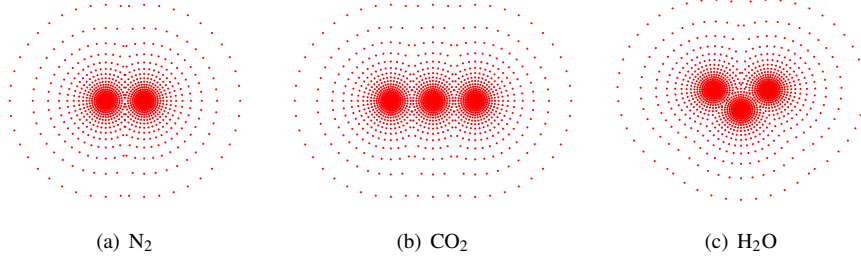


Figure 3: 2D sketches of molecular grids used in the Voronoi-cell finite difference method.

the density-functional theory (DFT) [55]. The DFT states the total energy can be obtained by energy functional [56],

$$E_{\text{total}} = E[\rho] = T_s[\rho] + J[\rho] + E_{\text{ne}}[\rho] + E_{\text{xc}}[\rho_{\uparrow}, \rho_{\downarrow}], \quad (33)$$

where ρ is the total density, and \uparrow and \downarrow indicate spin-up and spin-down, respectively. $T_s[\rho]$ is the noninteracting kinetic energy functional, $J[\rho]$ is the classical electron–electron repulsion energy functional, and $E_{\text{ne}}[\rho]$ is the nucleus–electron Coulomb interaction energy functional.

$$J[\rho] = \frac{1}{2} \iint \frac{\rho(\mathbf{r})\rho(\mathbf{r}')}{|\mathbf{r} - \mathbf{r}'|} d\mathbf{r}d\mathbf{r}', \quad (34)$$

$$E_{\text{ne}}[\rho] = \int \sum_A \frac{Z_A \rho(\mathbf{r})}{|\mathbf{r} - \mathbf{R}_A|} d\mathbf{r}, \quad (35)$$

where \mathbf{R}_A and Z_A are the nuclear position and charge of the A -th nucleus, respectively. $E_{\text{xc}}[\rho_{\uparrow}, \rho_{\downarrow}]$ is the exchange–correlation energy functional whose exact form is unknown and it needs to be approximated.

In the Kohn–Sham DFT formulation [57], one solves the Schrödinger-like equation for N -electron systems,

$$\left[-\frac{1}{2} \nabla^2 + u_{\text{eff},\sigma}(\mathbf{r}) \right] \psi_{i\sigma}(\mathbf{r}) = \varepsilon_{i\sigma} \psi_{i\sigma}(\mathbf{r}), \quad (i = 1, 2, \dots, N_{\sigma}) \quad (36)$$

where i and σ are the orbital and spin indexes, respectively. The spin density is given by

$$\rho_{\sigma}(\mathbf{r}) = \sum_{i=1}^{N_{\sigma}} |\psi_{i\sigma}(\mathbf{r})|^2, \quad (37)$$

and the total density is given by

$$\rho(\mathbf{r}) = \sum_{\sigma} \rho_{\sigma}(\mathbf{r}) = \rho_{\uparrow}(\mathbf{r}) + \rho_{\downarrow}(\mathbf{r}). \quad (38)$$

The effective potential $u_{\text{eff},\sigma}(\mathbf{r})$ consists of three terms,

$$u_{\text{eff},\sigma}(\mathbf{r}) = u_{\text{ne}}(\mathbf{r}) + u_{\text{h}}(\mathbf{r}) + u_{\text{xc},\sigma}(\mathbf{r}). \quad (39)$$

In the framework of VFD, detailed expressions for each term are as follows.

(i) Nucleus–electron potential: The Coulomb interaction between the electron and nuclei is given by

$$u_{\text{ne}}(\mathbf{r}) = \sum_A \frac{Z_A}{|\mathbf{r} - \mathbf{R}_A|}. \quad (40)$$

Its matrix form in VFD is simply given by diagonal elements evaluated at each grid.

(ii) Hartree potential: The Hartree potential is given by the classical electron–electron repulsion,

$$u_{\text{h}}(\mathbf{r}) = \int \frac{\rho(\mathbf{r}')}{|\mathbf{r} - \mathbf{r}'|} d\mathbf{r}'. \quad (41)$$

Alternatively, it is computable by solving the Poisson equation,

$$\nabla^2 u_{\text{h}}(\mathbf{r}) = -4\pi\rho(\mathbf{r}). \quad (42)$$

Its discrete form \mathbf{u}_{h} is simply solvable by a linear system solution of the Laplacian matrix in VFD,

$$\mathbf{L}\mathbf{u}_{\text{h}} = -4\pi\boldsymbol{\rho}, \quad (43)$$

where \mathbf{u}_{h} and $\boldsymbol{\rho}$ are column vector forms of the Hartree potential and the total density represented in every grid.

$$\mathbf{u}_{\text{h}} = (\dots w_i \dots)^T; \quad w_i = u_{\text{h}}(\mathbf{r}_i), \quad (44)$$

$$\boldsymbol{\rho} = (\dots \rho_i \dots)^T; \quad \rho_i = \rho(\mathbf{r}_i). \quad (45)$$

Here \mathbf{L} is the VFD Laplacian matrix in Eq. (5). After substituting the similarity transformation of Eq. (12) into Eq. (43), one obtains the symmetric form,

$$\tilde{\mathbf{L}}\tilde{\mathbf{u}}_{\text{h}} = -4\pi\tilde{\boldsymbol{\rho}}, \quad (46)$$

where $\tilde{\mathbf{u}}_{\text{h}} = \mathbf{V}^{\frac{1}{2}}\mathbf{u}_{\text{h}}$ and $\tilde{\boldsymbol{\rho}} = \mathbf{V}^{\frac{1}{2}}\boldsymbol{\rho}$. The boundary conditions for the Hartree potential ($= Q/r$ where Q is the total charge of electrons) are easily incorporated within $\tilde{\mathbf{L}}$. Note that the Poisson equation is solved with the same local grid refinement as the Schrödinger equation or the Kohn–Sham equation. Even though molecular grids are introduced to capture the nucleus–electron Coulomb singularity, one can expect that they also take care of electron–electron Coulomb singularity because the total electronic density is localized near nuclear positions.

(iii) Exchange–correlation potential: The conventional exchange–correlation functionals, such as local spin-density approximation (LSDA) or generalized gradient approximation (GGA), contain spurious self-interaction energy [55] and they do not possess the correct long-range Coulombic ($-1/r$) behavior. To take into account the proper long-range potential and remove the self-interaction energy, we adopt the improved Leeuwen–Baerends (LB α) potential [58],

$$u_{\text{xc},\sigma}^{\text{LB}\alpha}(\mathbf{r}) = \alpha u_{\text{xc},\sigma}^{\text{LSDA}}(\mathbf{r}) + u_{\text{c},\sigma}^{\text{LSDA}}(\mathbf{r}) - \frac{\beta x_{\sigma}^2(\mathbf{r}) \rho_{\sigma}^{1/3}(\mathbf{r})}{1 + 3\beta x_{\sigma}(\mathbf{r}) \log(x_{\sigma}(\mathbf{r}) + \sqrt{x_{\sigma}^2(\mathbf{r}) + 1})}, \quad (47)$$

where $x_\sigma(\mathbf{r}) = |\nabla\rho_\sigma(\mathbf{r})|/\rho_\sigma^{4/3}(\mathbf{r})$. Note that α and β are two adjustable parameters in the $\text{LB}\alpha$ potential. $u_{x,\sigma}^{\text{LSDA}}$ and $u_{c,\sigma}^{\text{LSDA}}$ indicate the exchange and correlation potentials of LSDA, respectively, and we use the Perdew–Wang representation for the correlation functional [59]. To assure the asymptotic Coulombic tail of $-1/r$, the Fermi–Amaldi term is smoothly attached for the long-range distance [60]. By means of the VFD gradient operator in Eq. (19), $x_\sigma(\mathbf{r})$ at the i -th grid is computed by

$$x_\sigma(\mathbf{r}_i) = \frac{\sqrt{(g_i^{(x)})^2 + (g_i^{(y)})^2 + (g_i^{(z)})^2}}{\rho_\sigma^{4/3}(\mathbf{r}_i)}, \quad (48)$$

where $g_i^{(x)} = [\nabla\rho_\sigma(\mathbf{r}) \cdot \hat{\mathbf{e}}_x]_i = \sum_j G_{ij}^{(x)} \rho_\sigma(\mathbf{r}_j)$ and likewise for $g_i^{(y)}$ and $g_i^{(z)}$.

3.2. VFD electronic structure calculation of polyatomic molecules

The DFT formula with the self-interaction-correction term provides considerable improvement on the electronic structure of atoms and molecules. Analogue to Koopman’s theorem for the Hartree–Fock approximation, orbital energies from the Kohn–Sham equation in Eq. (36) are comparable to the experimental vertical ionization potentials [61]. In Table 1, we present orbital binding energies ($-\varepsilon$) of several small polyatomic molecules calculated by the VFD method with the LSDA and $\text{LB}\alpha$ potentials, in comparison with experiments and other calculations.

We use experimental equilibrium geometry for the bond length (R) and the bond angle (\angle):

- (i) N_2 : $R_{\text{NN}}=2.074$ a.u. [62],
- (ii) F_2 : $R_{\text{FF}}=2.668$ a.u. [62],
- (iii) CO_2 : $R_{\text{CO}}=2.196$ a.u. [63] and $\angle_{\text{OCO}}=180^\circ$,
- (iv) H_2O : $R_{\text{OH}}=1.810$ a.u. and $\angle_{\text{HOH}}=104.48^\circ$ [64],
- (v) NH_3 : $R_{\text{NH}}=1.913$ a.u. and $\angle_{\text{HNH}}=106.67^\circ$ [63],
- (vi) CH_4 : $R_{\text{CH}}=2.054$ a.u. [65] and $\angle_{\text{HCH}}=109.471^\circ$.

Computational parameters in the VFD method are $N_r=300$, $L=0.5$ a.u., $r_{\text{max}}=20$ a.u., and $l_{\text{max}}=25$ for all molecular cases. For $\text{LB}\alpha$ parameters, we use $\alpha=1.19$ and $\beta=0.01$ for all cases.

For LSDA, we compare the VFD values with results by the standard quantum chemistry program of the linear combination of atomic orbitals (LCAO), which are performed by GAMESS [66] with a large basis-set of aug-cc-pVQZ [67] that is nearly converged to the complete basis-set limit. The LSDA orbital energies computed by VFD are well agreed up to ~ 0.1 eV for valence orbitals and up to ~ 0.4 eV for core orbitals with large basis-set calculations.

For $\text{LB}\alpha$, we compare the VFD values with the results obtained by the generalized pseudospectral (GPS) method [30, 68], which provides machine accuracy for atoms and diatomic molecules [31]. For diatomic molecules, N_2 and F_2 , the $\text{LB}\alpha$ valence orbital energies by VFD are almost exactly matched with the GPS values [25], ensuring the numerical accuracy of the VFD method.

These $\text{LB}\alpha$ values are comparable with experimental vertical ionization potentials [69–75]. For outer valence orbitals,

$\text{LB}\alpha$ orbital energies computed by VFD are close to experimental values within ~ 0.9 eV. Note that conventional LSDA functional without the self-interaction correction cannot describe electronic structure and ionization potential correctly, i.e., LSDA valence orbital energies are too weakly bound for all molecules.

4. Exploration of strong-field electronic dynamics in polyatomic molecules by time-dependent density-functional theory with proper long-range potential

4.1. Application of TDVFD to time-dependent density-functional theory

We now consider the solution of a set of time-dependent Kohn–Sham equations for N -electron systems in the time-dependent density-functional theory (TDDFT) framework [76],

$$i \frac{\partial}{\partial t} \psi_{i\sigma}(\mathbf{r}, t) = \left[-\frac{1}{2} \nabla^2 + u_{\text{eff},\sigma}(\mathbf{r}, t) \right] \psi_{i\sigma}(\mathbf{r}, t), \quad (49)$$

$$(i = 1, 2, \dots, N_\sigma),$$

where the time-dependent effective potential is expressed by

$$u_{\text{eff},\sigma}(\mathbf{r}, t) = u_{\text{ne}}(\mathbf{r}) + u_{\text{h}}(\mathbf{r}, t) + u_{\text{xc},\sigma}(\mathbf{r}, t) + \mathbf{F}(t) \cdot \mathbf{r}. \quad (50)$$

The time-dependent Hartree potential is

$$u_{\text{h}}(\mathbf{r}, t) = \int \frac{\rho(\mathbf{r}', t)}{|\mathbf{r} - \mathbf{r}'|} d\mathbf{r}', \quad (51)$$

and for the time-dependent exchange–correlation potential we use the adiabatic approximation [22] with the $\text{LB}\alpha$ potential of Eq. (47),

$$u_{\text{xc},\sigma}(\mathbf{r}, t) = u_{\text{xc},\sigma}^{\text{LB}\alpha}[\rho_\sigma] \Big|_{\rho_\sigma=\rho_\sigma(\mathbf{r}, t)}. \quad (52)$$

The correct long-range asymptotic behavior of the $\text{LB}\alpha$ potential is crucial for proper DFT treatment of molecular excited and continuum states in strong-field electronic dynamics [21, 23–25, 77]. The last term $\mathbf{F}(t) \cdot \mathbf{r}$ is the interaction of an electron with a linearly-polarized external laser field.

To solve Eq. (49), we use the TDVFD method described in Sec. 2.4. In the split-operator technique, $\hat{H}_0(\mathbf{r})$ and $\hat{U}(\mathbf{r}, t)$ are given by

$$\hat{H}_0(\mathbf{r}) = -\frac{1}{2} \nabla^2 + u_{\text{eff},\sigma}(\mathbf{r}, 0), \quad (53)$$

$$\hat{U}(\mathbf{r}, t) = \mathbf{F}(t) \cdot \mathbf{r} + [u_{\text{xc},\sigma}(\mathbf{r}, t) - u_{\text{xc},\sigma}(\mathbf{r}, 0)] + [u_{\text{h}}(\mathbf{r}, t) - u_{\text{h}}(\mathbf{r}, 0)], \quad (54)$$

and the time-dependent wavefunction for each spin-orbital is propagated by Eq. (24). Through the TDDFT formulation solved by the TDVFD method, we can now explore strong-field electronic dynamics including all molecular spin-orbitals and continuum states.

From the TDDFT solutions, one can compute the time-dependent ionization probability of individual spin-orbital by

$$P_{i\sigma}(t) = 1 - N_{i\sigma}(t), \quad (55)$$

Table 1: Orbital binding energies computed with LSDA and $LB\alpha$ in comparison with experimental (EXP) vertical ionization potentials and other calculations. All values are in eV. LCAO: Linear combination of atomic orbitals computed by GAMESS [66] with aug-cc-pVQZ; GPS: Generalized pseudospectral method [25].

Molecule	Orbital	LSDA		$LB\alpha$		EXP [Ref.]
		LCAO	VFD	GPS	VFD	
N ₂	$3\sigma_g$	10.4	10.4	15.5	15.5	15.5 [69]
	$1\pi_u$	11.9	11.9	16.9	16.9	16.8 [69]
	$2\sigma_u$	13.4	13.5	18.5	18.5	18.6 [69]
	$2\sigma_g$	28.2	28.2		33.0	37.3 [69]
	$1\sigma_u$	380.0	380.1		402.8	409.9 [69]
	$1\sigma_g$	380.1	380.2		402.8	409.9 [69]
F ₂	$1\pi_g$	9.6	9.7	16.0	16.0	15.9 [70]
	$1\pi_u$	13.1	13.1	19.2	19.3	18.8 [70]
	$3\sigma_g$	15.8	15.8	21.9	21.9	21.1 [70]
	$2\sigma_u$	27.4	27.5		33.8	
	$2\sigma_g$	33.9	33.9		39.9	
	$1\sigma_u$	658.7	659.1		686.7	
	$1\sigma_g$	658.7	659.1		686.7	
CO ₂	$1\pi_g$	9.3	9.4		14.7	13.8 [71]
	$1\pi_u$	13.0	13.0		18.2	17.6 [71]
	$3\sigma_u$	12.8	12.8		18.2	18.1 [71]
	$4\sigma_g$	13.8	13.8		19.2	19.4 [71]
	$2\sigma_u$	28.2	28.1		33.3	36.9 [72]
	$3\sigma_g$	29.1	29.1		34.2	38.0 [72]
	$2\sigma_g$	271.1	271.1		291.7	297.5 [69]
	$1\sigma_u$	508.6	508.9		533.7	540.8 [69]
	$1\sigma_g$	508.6	508.9		533.7	540.8 [69]
	H ₂ O	$1b_1$	7.4	7.4		12.5
$3a_1$		9.4	9.4		14.5	14.8 [73]
$1b_2$		13.3	13.3		18.2	18.7 [73]
$2a_1$		25.2	25.2		30.1	32.4 [73]
$1a_1$		506.4	506.6		531.0	539.7 [69]
NH ₃	$3a_1$	6.3	6.3		10.9	10.8 [74]
	$1e$	11.3	11.4		15.9	16.0 [74]
	$2a_1$	21.1	21.1		25.6	27.7 [74]
	$1a_1$	376.6	376.7		398.7	405.6 [69]
CH ₄	$1t_2$	9.5	9.5		13.9	13.6 [75]
	$2a_1$	17.0	17.0		21.3	22.9 [75]
	$1a_1$	265.5	265.6		285.4	290.7 [69]

where

$$N_{i\sigma}(t) = \langle \psi_{i\sigma}(\mathbf{r}, t) | \psi_{i\sigma}(\mathbf{r}, t) \rangle \quad (56)$$

is the population or survival probability of the spin-orbital, which is decreasing as a function of t due to the absorber [29] to prevent spurious reflections at radial boundary and to filter out the ionized wave packet. The total ionization probability P after one pulse ($t = T$) can be calculated by

$$P = 1 - \prod_{i\sigma} [1 - P_{i\sigma}(T)]. \quad (57)$$

In the limit of small $P_{i\sigma}(T)$, Eq. (57) is reduced to the sum of individual ionization probabilities,

$$P \approx \sum_{i\sigma} P_{i\sigma}(T). \quad (58)$$

4.2. Orientation dependence of multiphoton ionization of N_2

We perform TDDFT calculations of N_2 with arbitrary field-molecule orientation by means of the TDVFD method. The ground-state electronic configuration of N_2 is

$$[\text{core}](2\sigma_g)^2(2\sigma_u)^2(1\pi_u)^4(3\sigma_g)^2,$$

where [core] is $(1\sigma_g)^2(1\sigma_u)^2$ that corresponds to $1s$ orbitals of two N's. All orbitals except the core orbitals participate in the time-propagation.

For time-dependent solutions with the TDVFD method, the most time consuming part is Eq. (29), involving the matrix-vector multiplication. In the VFD and TDVFD schemes, the matrix size is identical to the total number of grid points. Table 2 shows $LB\alpha$ orbital binding energies of N_2 with smaller number of grids than one used in Table 1: $N_r=80$, $L=2$ a.u., $r_{\max}=40$ a.u., and $l_{\max}=12$, corresponding to the total number of grids $N_{\text{tot}}=21,164$. For $LB\alpha$ parameters, $\alpha=1.24$ is used. One can see that $LB\alpha$ orbital energies with a small number of grids still reproduce the electronic structure of N_2 in good agreement with experiments. Based on this electronic structure with the matrix size of $N_{\text{tot}}=21,164$, we are able to carry out time-dependent calculations with a reasonable computation time.

Table 2: Orbital binding energies (in eV) of N_2 computed by VFD with a small number of grids.

Orbital	VFD/ $LB\alpha$	EXP [Ref.]
$3\sigma_g$ (HOMO)	15.5	15.5 [69]
$1\pi_u$ (HOMO-1)	17.0	16.8 [69]
$2\sigma_u$ (HOMO-2)	19.0	18.6 [69]
$2\sigma_g$	33.3	37.3 [69]
$1\sigma_u$	410.8	409.9 [69]
$1\sigma_g$	410.8	409.9 [69]

In order to examine electronic dynamics as a function of the angle between the polarization of the laser field and the orientation of aligned N_2 , we define the orientation angle as shown in

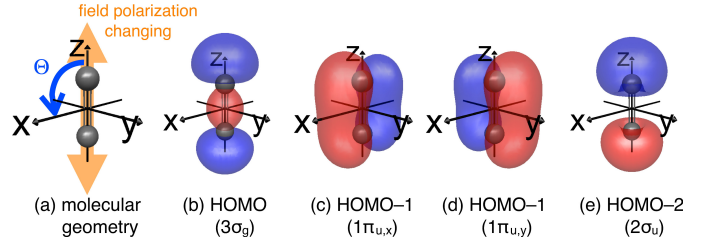


Figure 4: Molecular geometry and molecular orbital pictures of N_2 . The principal axis is the z -axis and the molecular geometry is fixed. Two nitrogen atoms (gray ball) are located in the z -axis. The field polarization axis with respect to the principal axis changes toward the x -axis (Θ).

Fig. 4(a). Without loss of generality, we assume that the molecular axis coincides with the z -axis and the polarization vector of the external field lies in the xz -plane, then $\mathbf{F}(t) \cdot \mathbf{r}$ is given by

$$\mathbf{F}(t) \cdot \mathbf{r} = F(t)(x \sin \Theta + z \cos \Theta), \quad (59)$$

where Θ is the orientation angle between the molecular axis and the field polarization axis.

For the sine-squared pulse envelope, we use

$$F(t) = F_0 \sin^2\left(\frac{\pi t}{T}\right) \sin \omega t, \quad (60)$$

where F_0 is the peak field amplitude, ω is the carrier frequency, and T is the pulse duration. During the time-propagation, we use the radial-based absorber function [29] as

$$w(r_c) = \cos^{\frac{1}{4}}\left[\frac{\pi(r_c - r_0)}{2(r_1 - r_0)}\right] \quad \text{for } r_0 \leq r_c \leq r_1, \quad (61)$$

where r_c is a radial distance from the closest nucleus. For computational parameters of time-dependent problems, we use $\omega=0.0556$ a.u. corresponding to the wavelength 800 nm, $T=20$ optical cycles (o.c.), $\Delta t=0.001$ o.c., $r_0=15$ a.u., and $r_1=25$ a.u. For $T=20$ o.c. calculation (20,000 time iterations in total), the computation time takes about 10.5 hours on the lab workstation equipped with two Intel X5355 CPUs.

Figures 4(b)–(e) illustrate individual orbital pictures of N_2 obtained by GAMESS [66] and MacMolPlt [78]. HOMO ($3\sigma_g$) and HOMO-2 ($2\sigma_u$) lie along with the z -axis and two degenerate HOMO-1 ($1\pi_{u,x}$ and $1\pi_{u,y}$) lie in the xz - and yz -planes. Energetically, the orbital of less ionization potential tends to be more ionized. Thus HOMO is usually expected to be the most dominant portion in the total ionization probability. However, the ionization process is also related to the molecular orbital symmetry [25, 31, 77, 79]. When the linearly-polarized laser field is applied to the z -axis (parallel, $\Theta=0^\circ$), HOMO and HOMO-2 can be more perturbed and ionized than other orbitals because the induced dipole change of σ -symmetry is preferable along with this field polarization parallel to the molecular axis [19]. On the other hand, when the field is applied to the x -axis (perpendicular, $\Theta=90^\circ$), HOMO-1 (only $1\pi_{u,x}$ in this case) symmetry is along with the field polarization. Therefore, we expect that the orientation dependence of MPI is reflected by individual orbital symmetries.

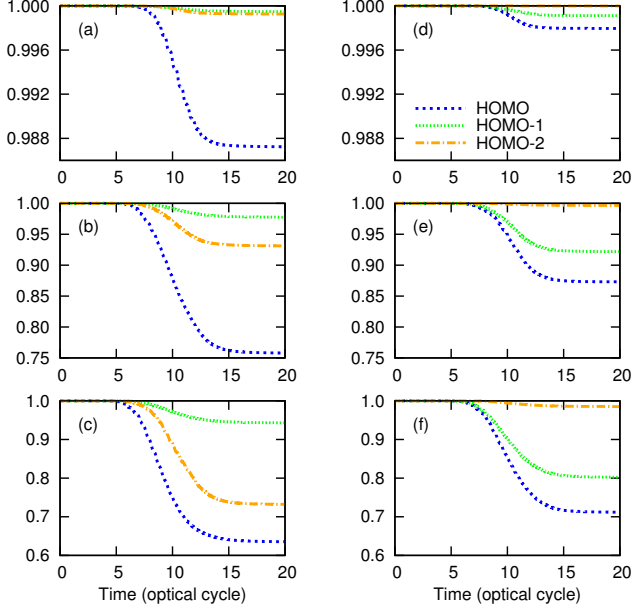


Figure 5: Plots of the time-dependent electron population $N_{i\sigma}(t)$ of individual spin-orbital of N_2 . The laser peak intensities are 10^{14} W/cm 2 in (a) and (d), 3×10^{14} W/cm 2 in (b) and (e), and 5×10^{14} W/cm 2 in (c) and (f). The field-molecule orientation angles are $\Theta=0^\circ$ for (a)–(c) and $\Theta=90^\circ$ for (d)–(f). The legend in (d) is for all plots.

In Fig. 5, we plot time-dependent electron population $N_{i\sigma}(t)$ of individual N_2 spin-orbital in the parallel [Fig. 5(a)–(c)] and perpendicular [Fig. 5(d)–(f)] cases. The peak intensities are 10^{14} W/cm 2 in Fig. 5(a) and (d); 3×10^{14} W/cm 2 in Fig. 5(b) and (e); and 5×10^{14} W/cm 2 in Fig. 5(c) and (f). In the parallel case ($\Theta=0^\circ$), HOMO exhibits the most dominant contribution to the total ionization and HOMO–2 contribution is also increasing as the intensity increases. On the other hand, HOMO–1 contribution is increasing as the intensity increases in the perpendicular case ($\Theta=90^\circ$) due to the orbital symmetry of π_u . Note that HOMO contribution is still dominant in both cases.

Figure 6 shows the orientation dependence of ionization probabilities of N_2 with 800 nm and 2×10^{14} W/cm 2 as a function of the field-molecule orientation angle. Note that larger angular grids are used ($l_{\max}=15$) in calculations to plot individual orbital ionization probabilities in Fig. 6 because of a possible resonance between HOMO and HOMO–1. The total ionization probability in the polar plot (left panel) looks like a dumbbell shape in accord with experiments [17]. The ionization probabilities of individual orbitals (right panel) illustrates importance of multi-electron effects between HOMO and HOMO–1. For $\Theta=15\text{--}40^\circ$, HOMO–1 contribution is larger than HOMO contribution. Thus, both HOMO and HOMO–1 contribute to this dumbbell shape of the orientation dependent plot of the total ionization probability. These comparable contributions from HOMO and HOMO–1 are explained by a small orbital energy difference and a strong coupling between HOMO and HOMO–1. In Table 2, calculated difference between HOMO and HOMO–1 is only 1.5 eV, which is relatively small in comparison with other molecules in Table 1. Moreover, this energy gap is very close to the photon energy (1.55 eV) correspond-

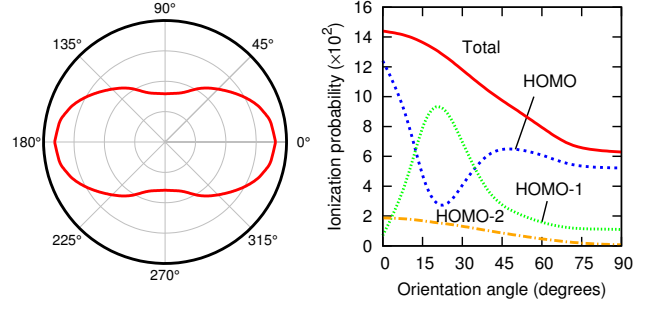


Figure 6: Orientation dependence of total ionization probability (left panel) and individual ionization probability of multiple orbitals (right panel) of N_2 with 800 nm and 2×10^{14} W/cm 2 .

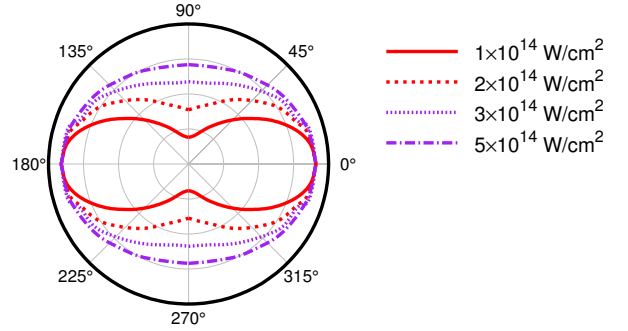


Figure 7: Effects of laser intensity on the orientation dependence of total ionization probability of N_2 .

ing to the carrier wavelength of 800 nm. A transition between HOMO ($3\sigma_g$) and HOMO–1 ($1\pi_u$) is forbidden in the parallel case ($\Theta=0^\circ$) but allowed in other angles, so it leads to a possible one-photon resonance between HOMO and HOMO–1. This phenomenon is also theoretically predicted in MPI and HHG of N_2 in the 800 nm laser field [80].

Next, we consider effects of laser intensity on the orientation dependent patterns in Fig. 7. The peak intensity of laser pulses is varying from 10^{14} to 5×10^{14} W/cm 2 , and the wavelength is fixed at 800 nm. All data sets are normalized to their maximum value. As the intensity increases, the polar plot becomes less anisotropic [25] because at higher intensity all orbitals participate in the ionization process, thus losing a characteristic pattern of each orbital.

4.3. Orientation dependence of multiphoton ionization of H_2O

We perform TDDFT calculations of H_2O with arbitrary field-molecule orientation by means of the TDVFD method. The ground-state electronic configuration of H_2O is

$$[\text{core}](2a_1)^2(1b_2)^2(3a_1)^2(1b_1)^2,$$

where [core] is $(1a_1)^2$ that corresponds to O $1s$ orbital. All orbitals except the core orbital participate in the time-propagation. Table 3 lists $LB\alpha$ orbital binding energies with a small number of grids and $\alpha=1.21$ is used. The grid parameters are $N_r=80$,

$L=2$ a.u., $r_{\max}=40$ a.u., and $l_{\max}=10$, which provide $N_{\text{tot}}=20,022$ for the triatomic H_2O molecule. For the time-propagation of $T=20$ o.c., the computation time is about 9 hours on the same workstation mentioned in Sec. 4.2.

Table 3: Orbital binding energies (in eV) of H_2O computed by VFD with a small number of grids.

Orbital	VFD/LB α	EXP [Ref.]
$1b_1$ (HOMO)	12.6	12.6 [73]
$3a_1$ (HOMO-1)	14.6	14.8 [73]
$1b_2$ (HOMO-2)	18.2	18.7 [73]
$2a_1$	30.5	32.4 [73]
$1a_1$	540.5	539.7 [69]

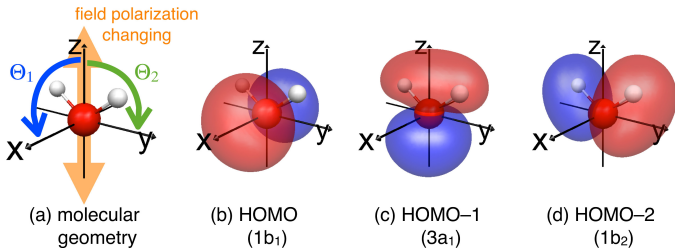


Figure 8: Molecular geometry and molecular orbital pictures of H_2O . The principal axis is the z -axis and the molecular geometry is fixed. Oxygen atom (red ball) and two hydrogen atoms (white ball) are contained in the yz -plane. The field polarization axis with respect to the principal axis changes toward the x -axis (Θ_1) or the y -axis (Θ_2).

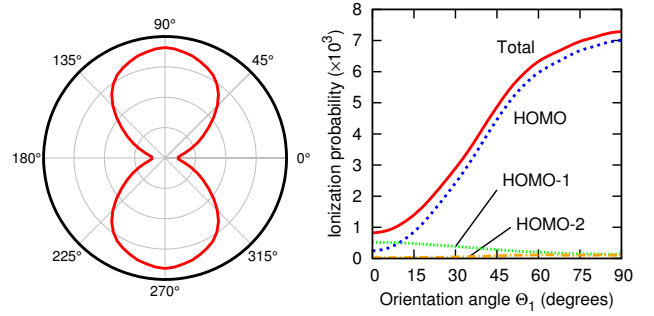
Figure 8 depicts orbital pictures of H_2O with the molecular geometry. The principal axis is the z -axis and the molecular geometry is fixed. All atoms of H_2O are contained in the yz -plane. HOMO ($1b_1$), HOMO-1 ($3a_1$), and HOMO-2 ($1b_2$) have atomic p -orbital-like characters along with the x -, z -, and y -axis, respectively. With respect to the fixed molecular frame of H_2O , the field polarization direction can change in two different ways as shown in Fig. 8(a). First, the angle changes from the z -axis toward the x -axis (denoted by Θ_1). The interaction between the electron and the field is given by

$$\mathbf{F}(t) \cdot \mathbf{r} = F(t)(x \sin \Theta_1 + z \cos \Theta_1). \quad (62)$$

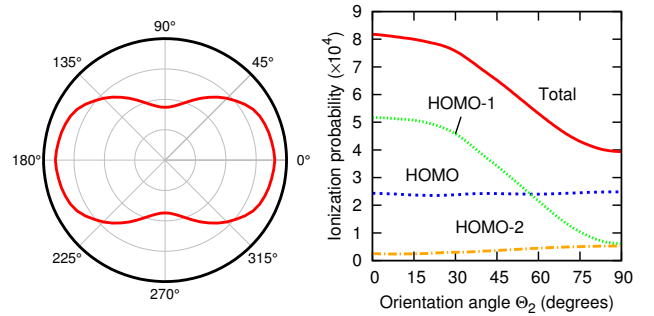
Second, the angle changes from the z -axis toward the y -axis (denoted by Θ_2). Then,

$$\mathbf{F}(t) \cdot \mathbf{r} = F(t)(y \sin \Theta_2 + z \cos \Theta_2). \quad (63)$$

According to orbital pictures in Figs. 8(b)–(d), there is no orientation dependence when the field polarization varies within the nodal plane of each orbital, while the orientation dependence maximizes when the field polarization approaches the p -orbital-like polarization of each orbital. In other words, increment of Θ_1 triggers to maximize HOMO ionization, to minimize HOMO-1 ionization, and no effects on HOMO-2 ionization. On the other hand, increment of Θ_2 causes no effects on HOMO ionization, to minimize HOMO-1 ionization, and



(a) Orientation changes of Θ_1



(b) Orientation changes of Θ_2

Figure 9: Orientation dependence of total ionization probability (left panel) and individual ionization probability of multiple orbitals of H_2O with 800 nm and 5×10^{13} W/cm².

to maximize HOMO-2 ionization. Consequently, it provides feasibility to selectively probe the MPI processes of individual orbitals in aligned H_2O .

Figure 9 shows the orientation dependence of total ionization probability of H_2O with 800 nm and 5×10^{13} W/cm² as a function of (a) Θ_1 and (b) Θ_2 . When Θ_1 changes, the orientation dependence of total ionization probability mostly follows the pattern of HOMO as shown in Fig. 9(a). On the other side, the appearance of the orientation dependence is dramatically changed when Θ_2 changes. Since HOMO has the nodal plane of the yz -plane, the change of Θ_2 in the yz -plane does not affect HOMO ionization. Thus the overall pattern of the orientation dependence of total ionization probability is dominantly determined by HOMO-1 as shown in Fig. 9(b). To our knowledge, this is the first prediction of the dominant contribution from HOMO-1 to the overall orientation dependent pattern of MPI.

5. Conclusion

In this paper, we introduced a new time-dependent Voronoi-cell finite difference (TDVFD) method to investigate multiphoton ionization of polyatomic molecules in intense ultrashort laser fields. Based on the Voronoi diagram and natural neighboring relations, the method provides simple expressions for

the discrete Laplacian and gradient operators on highly adaptive grids suitable for polyatomic molecules. It combines an efficient and accurate time-propagation method of the split-operator technique in the *energy* representation. The method is applied to solve the *self-interaction-free* density-functional theory equations for accurate electronic structures of polyatomic molecules, and the time-dependent density-functional theory equations for strong-field electronic dynamics in polyatomic molecules including all spin-orbitals and continuum states.

By means of the proposed TDVFD method, we presented *ab initio* time-dependent density-functional studies of multiphoton ionization (MPI) of N_2 and H_2O in intense ultrashort laser fields with arbitrary orientation, including electron correlation and multi-electron responses. Our results showed that the orientation dependence of MPI is determined by the symmetries and dynamics of multiple orbitals. For N_2 , the orientation dependent pattern of MPI is reflected by contributions from HOMO and HOMO-1. For H_2O , the contribution from HOMO-1 dominates the overall orientation dependent pattern of MPI when the laser field polarization is varied. This feature emphasizes importance of multiple orbital contributions to the MPI processes. Also it enables us to selectively probe individual orbital in strong-field electronic dynamics.

Finally, we would like to conclude with some open questions regarding the TDVFD method and time-dependent density-functional theory (TDDFT). The TDVFD method presented here is the first-order scheme in the sense that it considers only nearest natural neighboring grids in VFD. Although it is shown that the first-order scheme realizes accurate calculations combined with highly adaptive grids, there will be more rooms for improvement toward the high-order scheme, allowing exploration of complicated molecules and elaborate strong-field phenomena such as high harmonic generation in the future work. As for TDDFT, since the exact steady-state and time-dependent exchange-correlation (xc) energy functional is unknown, further refinement of the xc energy functional, such as more rigorous treatment of the self-interaction correction for the molecular systems as well as the implementation of the derivative discontinuity, etc., will be required for the accurate treatment of other important chemical and physical problems, such as charge transfer processes and double and multiple electron ionization, etc., in the future.

Acknowledgments

This work is partially supported by the Chemical Sciences, Geosciences and Biosciences Division of the Office of Basic Energy Sciences, Office of Sciences, U.S. Department of Energy and by U.S. National Science Foundation. We also would like to acknowledge the partial support of National Science Council of Taiwan (No. 97-2112-M-002-003-MY3), and National Taiwan University (No. 97R0066).

References

[1] A. Scrinzi, M.Y. Ivanov, R. Kienberger, D.M. Villeneuve, *J. Phys. B: At. Mol. Opt. Phys.* 39 (2006) R1.

[2] P.B. Corkum, F. Krausz, *Nat. Phys.* 3 (2007) 381.
 [3] M. Hentschel, R. Kienberger, Ch. Spielmann, G.A. Reider, N. Milosevic, T. Brabec, P. Corkum, U. Heinzmann, M. Drescher, F. Krausz, *Nature* 414 (2001) 509.
 [4] M. Drescher, M. Hentschel, R. Kienberger, G. Tempea, Ch. Spielmann, G.A. Reider, P.B. Corkum, F. Krausz, *Science* 291 (2001) 1923.
 [5] A. Baltuška, Th. Udem, M. Uiberacker, M. Hentschel, E. Goulielmakis, C. Gohle, R. Holzwarth, V.S. Yakovlev, A. Scrinzi, T.W. Hänsch, F. Krausz, *Nature* 421 (2003) 611.
 [6] J.J. Carrera, X.M. Tong, S.I. Chu, *Phys. Rev. A* 74 (2006) 023404.
 [7] R. Kienberger, M. Hentschel, M. Uiberacker, Ch. Spielmann, M. Kitzler, A. Scrinzi, M. Wieland, Th. Westerwalbesloh, U. Kleineberg, U. Heinzmann, M. Drescher, F. Krausz, *Science* 297 (2002) 1144.
 [8] S. Baker, J.S. Robinson, C.A. Haworth, H. Teng, R.A. Smith, C.C. Chirilă, M. Lein, J.W.G. Tisch, J.P. Marangos, *Science* 312 (2006) 424.
 [9] M. Uiberacker, Th. Uphues, M. Schultze, A.J. Verhoef, V. Yakovlev, M.F. Kling, J. Rauschenberger, N.M. Kabachnik, H. Schröder, M. Lezius, K.L. Kompa, H.-G. Müller, M.J.J. Vrakking, S. Hendel, U. Kleineberg, U. Heinzmann, M. Drescher, F. Krausz, *Nature* 446 (2007) 627.
 [10] M. Drescher, M. Hentschel, R. Kienberger, M. Uiberacker, V. Yakovlev, A. Scrinzi, Th. Westerwalbesloh, U. Kleineberg, U. Heinzmann, F. Krausz, *Nature* 419 (2002) 803.
 [11] J. Itatani, J. Levesque, D. Zeidler, H. Niikura, H. Pepin, J.C. Kieffer, P.B. Corkum, D.M. Villeneuve, *Nature* 432 (2004) 867.
 [12] P.H. Bucksbaum, *Science* 317 (2007) 766.
 [13] X.M. Tong, Z.X. Zhao, C.D. Lin, *Phys. Rev. A* 66 (2002) 033402.
 [14] J. Muth-Böhm, A. Becker, F.H.M. Faisal, *Phys. Rev. Lett.* 85 (2000) 2280.
 [15] M.J. DeWitt, E. Wells, R.R. Jones, *Phys. Rev. Lett.* 87 (2001) 153001.
 [16] E. Wells, M.J. DeWitt, R.R. Jones, *Phys. Rev. A* 66 (2002) 013409.
 [17] D. Pavičić, K.F. Lee, D.M. Rayner, P.B. Corkum, D.M. Villeneuve, *Phys. Rev. Lett.* 98 (2007) 243001.
 [18] I. Thomann, R. Lock, V. Sharma, E. Gagnon, S.T. Pratt, H.C. Kapteyn, M.M. Murnane, W. Li, *J. Phys. Chem. A* 112 (2008) 9382.
 [19] B.K. McFarland, J.P. Farrell, P.H. Bucksbaum, M. Gühr, *Science* 322 (2008) 1232.
 [20] W. Li, X. Zhou, R. Lock, S. Patchkovskii, A. Stolow, H.C. Kapteyn, M.M. Murnane, *Science* 322 (2008) 1207.
 [21] S.I. Chu, *J. Chem. Phys.* 123 (2005) 062207.
 [22] X.M. Tong, S.I. Chu, *Phys. Rev. A* 57 (1998) 452.
 [23] X. Chu, S.I. Chu, *Phys. Rev. A* 70 (2004) 061402(R).
 [24] J. Heslar, J.J. Carrera, D.A. Telnov, S.I. Chu, *Int. J. Quant. Chem.* 107 (2007) 3159.
 [25] D.A. Telnov, S.I. Chu, *Phys. Rev. A* 79 (2009) 041401(R).
 [26] P. Krause, T. Klamroth, P. Saalfrank, *J. Chem. Phys.* 127 (2007) 034107; H.B. Schlegel, S.M. Smith, X. Li, *J. Chem. Phys.* 126 (2007) 244110.
 [27] J. Zanghellini, M. Kitzler, T. Brabec, A. Scrinzi, *J. Phys. B: At. Mol. Opt. Phys.* 37 (2004) 763; M. Nest, T. Klamroth, P. Saalfrank, *J. Chem. Phys.* 122 (2005) 124102.
 [28] K.C. Kulander (Ed.), *Time-Dependent Methods for Quantum Dynamics*, North-Holland, Amsterdam, 1991, reprinted from *Comput. Phys. Commun.* 63 (1991) nos. 1-3.
 [29] X.M. Tong, S.I. Chu, *Chem. Phys.* 217 (1997) 119.
 [30] X. Chu, S.I. Chu, *Phys. Rev. A* 63 (2001) 023411.
 [31] D.A. Telnov, S.I. Chu, *Phys. Rev. A* 76 (2007) 043412.
 [32] G. Voronoï, *J. Reine Angew. Math.* 134 (1908) 198.
 [33] A. Okabe, B. Boots, K. Sugihara, S.N. Chiu, *Spatial Tessellations: Concepts and Applications of Voronoi Diagrams*, 2nd Edition, John Wiley & Sons, Chichester, 2000.
 [34] F. Aurenhammer, *ACM Comput. Surv.* 23 (1991) 345.
 [35] J. Braun, M. Sambridge, *Nature* 376 (1995) 655.
 [36] N. Sukumar, B. Moran, A.Y. Semenov, V.V. Belikov, *Int. J. Numer. Meth. Engng* 50 (2001) 1.
 [37] E. Cueto, N. Sukumar, B. Calvo, M.A. Martínez, J. Cegoñino, M. Doblaré, *Arch. Comput. Meth. Engng.* 10 (2003) 307.
 [38] N. Sukumar, *Int. J. Numer. Meth. Engng* 57 (2003) 1.
 [39] N. Sukumar, J.E. Bolander, *Comput. Model. Eng. Sci.* 4 (2003) 691.
 [40] N. Sukumar, R.W. Wright, *Int. J. Numer. Meth. Engng* 70 (2007) 181.
 [41] M. Griebel, M.A. Schweitzer (Eds.), *Meshfree Methods for Partial Differential Equations*, Springer, Berlin, 2003.
 [42] S.-K. Son, in preparation.
 [43] R. Sibson, *Math. Proc. Cambridge Philos. Soc.* 87 (1980) 151.

- [44] C.B. Barber, D.P. Dobkin, H. Huhdanpaa, *ACM Trans. Math. Software* 22 (1996) 469.
- [45] G.B. Arfken, H.J. Weber, *Mathematical Methods for Physicists*, 5th Edition, Harcourt/Academic Press, San Diego, 2001.
- [46] J.M. Hyman, R.J. Knapp, J.C. Scovel, *Physica D* 60 (1992) 112.
- [47] R.B. Lehoucq, D.C. Sorensen, C. Yang, *ARPACK Users' Guide: Solution of Large-Scale Eigenvalue Problems with Implicitly Restarted Arnoldi Methods*, SIAM, Philadelphia, 1998.
- [48] O. Schenk, K. Gärtner, *Elect. Trans. Numer. Anal.* 23 (2006) 158.
- [49] D. González, E. Cueto, M.A. Martínez, M. Doblaré, *Int. J. Numer. Meth. Engng* 60 (2004) 2077.
- [50] J. Lu, J. Qian, W. Han, *Int. J. Numer. Meth. Engng* 74 (2008) 619.
- [51] M.R. Hermann, J.A. Fleck, Jr., *Phys. Rev. A* 38 (1988) 6000.
- [52] M.D. Feit, J.A. Fleck, Jr., A. Steiger, *J. Comput. Phys.* 47 (1982) 412.
- [53] V.I. Lebedev, *Comput. Math. Math. Phys.* 16 (1976) 10.
- [54] R.S. Womersley, I.H. Sloan, *Adv. Comput. Math.* 14 (2001) 195.
- [55] R.G. Parr, W. Yang, *Density-Functional Theory of Atoms and Molecules*, Oxford University Press, New York, 1989.
- [56] P. Hohenberg, W. Kohn, *Phys. Rev.* 136 (1964) B864.
- [57] W. Kohn, L.J. Sham, *Phys. Rev.* 140 (1965) A1133.
- [58] P.R.T. Schipper, O.V. Gritsenko, S.J.A. van Gisbergen, E.J. Baerends, *J. Chem. Phys.* 112 (2000) 1344.
- [59] J.P. Perdew, Y. Wang, *Phys. Rev. B* 45 (1992) 13244.
- [60] S. Liu, R.G. Parr, *J. Comput. Chem.* 20 (1999) 2.
- [61] D.P. Chong, O.V. Gritsenko, E.J. Baerends, *J. Chem. Phys.* 116 (2002) 1760.
- [62] K.P. Huber, G. Herzberg, *Molecular Spectra and Molecular Structure, IV. Constants of Diatomic Molecules*, Van Nostrand, New York, 1979.
- [63] G. Herzberg, *Molecular Spectra and Molecular Structure, III. Electronic Spectra and Electronic Structure of Polyatomic Molecules*, Van Nostrand, New York, 1966.
- [64] A.R. Hoy, P.R. Bunker, *J. Mol. Spectrosc.* 74 (1979) 1.
- [65] E. Hirota, *J. Mol. Spectrosc.* 77 (1979) 213.
- [66] M.W. Schmidt, K.K. Baldridge, J.A. Boatz, S.T. Elbert, M.S. Gordon, J.H. Jensen, S. Koseki, N. Matsunaga, K.A. Nguyen, S. Su, T.L. Windus, M. Dupuis, J.A. Montgomery, Jr., *J. Comput. Chem.* 14 (1993) 1347.
- [67] T.H. Dunning, Jr., *J. Chem. Phys.* 90 (1989) 1007.
- [68] G.H. Yao, S.I. Chu, *Chem. Phys. Lett.* 204 (1993) 381.
- [69] K. Siegbahn, C. Nordling, G. Johansson, J. Hedman, P.F. Heden, K. Hamrin, U. Gelius, T. Bergmark, L.O. Werme, R. Manne, Y. Baer, *ESCA Applied to Free Molecules*, North-Holland Pub. Co., Amsterdam, 1969.
- [70] G. Bieri, L. Åsbrink, W. von Niessen, *J. Electron Spectrosc. Relat. Phenom.* 23 (1981) 281.
- [71] D.W. Turner, C. Baker, A.D. Baker, C.R. Brundle, *Molecular Photoelectron Spectroscopy*, Wiley-interscience, London, 1970.
- [72] H.J. Freund, H. Kossmann, V. Schmidt, *Chem. Phys. Lett.* 123 (1986) 463.
- [73] C.G. Ning, B. Hajgató, Y.R. Huang, S.F. Zhang, K. Liu, Z.H. Luo, S. Knippenberg, J.K. Deng, M.S. Deleuze, *Chem. Phys.* 343 (2008) 19.
- [74] G. Bieri, L. Åsbrink, W. von Niessen, *J. Electron Spectrosc. Relat. Phenom.* 27 (1982) 129.
- [75] G. Bieri, L. Åsbrink, *J. Electron Spectrosc. Relat. Phenom.* 20 (1980) 149.
- [76] E. Runge, E.K.U. Gross, *Phys. Rev. Lett.* 52 (1984) 997.
- [77] S.-K. Son, S.I. Chu, *Phys. Rev. A* 80 (2009) 011403(R).
- [78] B.M. Bode, M.S. Gordon, *J. Mol. Graphics Mod.* 16 (1998) 133.
- [79] G.L. Kamta, A.D. Bandrauk, *Phys. Rev. A* 74 (2006) 033415.
- [80] D.A. Telnov, S.I. Chu, *Phys. Rev. A* (submitted).